

Ionospheric Disturbances produced by the 2019 Caribbean Meteoroid

Jorge Tarango-Yong^{a,*}, Mario Rodriguez-Martinez^{a,**}, Raul Gutiérrez-Zalapa^{a,1}

^a*Escuela Nacional de Estudios Superiores, UNAM, campus Morelia, Antigua Carretera a Pátzcuaro No. 8701 Col. Ex Hacienda de San José de la Huerta, Morelia, Michoacán, 58190, México*

Abstract

Asteroids and other objects impact the Earth every day and cause different harm degree: from the smallest which perturb lightly the atmosphere to the biggest ones which cause global catastrophes. In this work we are studying the case of a meteoroid which hit the Earth in June 22th 2019 and was detected independently over the Caribbean Sea by U.S Goverment sensors and the Geostationary Lightning Mapper (GLM) and registered an impact energy of about 6 kt. This is the most energetic event registered by both databases simultaneously, and is an excellent opportunity to develop a method to study the Traveling Ionospheric Disturbances produced upon impact.

© 2022 COSPAR. Published by Elsevier Ltd All rights reserved.

Keywords: Space Sciences; Atmosphere ; Ionosphere ; UNAVCO

1. Introduction

Bolides impact the Earth every day, from the smallest ($d < 0.5$ m), which are destroyed when entering the atmosphere to the biggest and most rare events, where an asteroid with a diameter $d > 100$ m is almost unaffected by the atmosphere and is technically unable to slow them down. If their diameter is greater than 1 km the impact can be considered a global catastrophe (Dudorov & Eretnova, 2020). Some famous modern cases are the Tunguska event 1n 1908 (Wheeler & Mathias, 2019) and the Chelyabinsk event (Yang et al., 2014) in 2013.

Such events have been recently recorded in certain databases, such as the Center for Near Earth Objects Studies (CNEOS), Jet Propulsion Laboratory (JPL) and the Geostationary Lightning Mapper (GLM), publicly available at <https://cneos.jpl.nasa.gov/fireballs/> and <https://neo-bolide.ndc.nasa.gov/#/>, respectively.

We picked our interest in one certain event, that we nicknamed “the Caribbean Meteoroid”, because this meteoroid is the most energetic which appear in both databases and thus is

an interesting case for studying the potential Traveling Ionospheric Disturbances (TIDs) that could be produced. To do so, we collected RINEX data from nearby GPS stations from the UNAVCO network (also publicly available) and developed a method to detrend the resultant TEC series and estimate the TIDs propagation speed ... (The introduction also needs to be polished after getting the main results)

2. Data proccesing

2.1. Meteor location and trajectory

Data of the Caribbean meteoroid is available from the Geostationary Lightning Mapper (GLM) (Goodman et al., 2013) and the Center for Near Earth Object Studies (CNEOS) of the Jet Propulsion Laboratory (JPL) of the NASA. We used the interactive database of both projects, available at <https://neo-bolide.ndc.nasa.gov/#/> and <https://cneos.jpl.nasa.gov/fireballs/>. From these databases, we found basic physical parameters such as event coordinates, altitude, total velocity as well as its components, total radiated energy and calculated impact energy. These data are shown in table 1.

Row 7 shows the velocity components of the bolide. v_x is the velocity in the equatorial plane, positive towards the prime meridian, v_z is directed towards the celestial north pole and v_y

*Tel.: +52-443-476-5525;
 email: jorge.tarango@comunidad.unam.mx
 **email: m.rodriguez@enesmorelia.unam.mx

Table 1. List of meteor basic parameters. Source: <https://cneos.jpl.nasa.gov/fireballs/>

| | | |
|-------------------------------------|-------------------------|---------------------|
| Event date (yyyy-mm-dd) | 2019-06-22 | |
| Time (UT) | 21:25:48 | |
| Latitude (deg) | 14.9 | |
| Longitude (deg) | -66.2 | |
| Altitude (km) | 25.0 | |
| Velocity (km/s) | 14.9 | |
| Duration (seconds) | 4.873 | |
| Velocity components (km/s) | v_x v_y v_z | -13.4 6.0 2.5 |
| Total radiated energy (J) | 294.7×10^{10} | |
| Calculated Total Impact energy (kt) | 6 | |

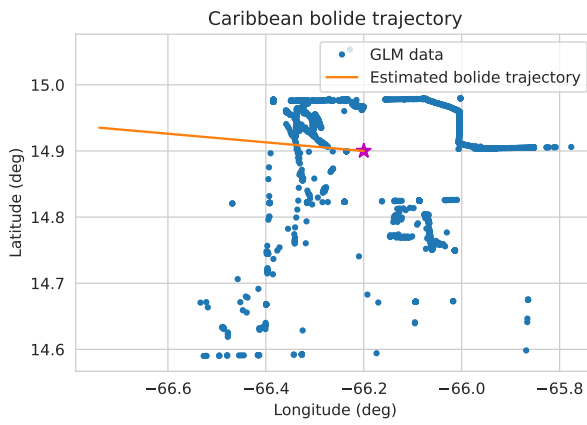


Fig. 1. In orange continuous line, the Caribbean bolide estimated trajectory using velocity components from table 1. In blue dots, GLM position records.

completes the right-handed coordinate system, see figure A.16 in appendix Appendix A.

From GLM data we know that the bolide was visible for 4.873 seconds. The trajectory using the data is shown in figure 1, among with the GLM records.

3. RINEX data

We collected RINEX data for event from 38 stations that surrounded the impact coordinates for the day of the event. Since the event occurred near 24:00 UT, we also obtained GPS data for the next day in case of there would be TIDs detected several hours after the fragmentation. We obtained TEC curves using the GOPI software and detrended the resulting time series for each receiver-satellite line of sight. Table D.4 shows the stations names, coordinates and proper citations.

The obtained RINEX files are compressed in Hatanaka format, developed at the Geographical Survey Institute by Y. Hatanaka (Kumar et al., 2012). From this files we may estimate the Slant Total Electron Content (sTEC) and the Vertical Total Electron Content (vTEC) which may be computed in the following way:

The Total Electron content along the integrated path of the link (s_i) at the frequency f_i can be inferred from the phase delay L_i of the frequency f_i (Emery & Camps, 2017):

$$L_i = s_i - \frac{40.3082 \text{ m}^3 \text{ s}^{-1}}{f_i^2} sTEC_i \quad (1)$$

Combining two observations at two different frequencies f_1 and f_2 we may obtain two different phase delays L_1 and L_2 and derive the TEC along the signal path:

$$sTEC = \frac{f_1^2 f_2^2 (L_1 - L_2)}{40.3082 \text{ m}^3 \text{ s}^{-1} (f_1^2 - f_2^2)} \quad (2)$$

In the other hand, the vertical Total Electron Content (vTEC) is computed from the sTEC as follows (Kumar et al., 2012). In figure 2 we illustrate the satellite-receiver path and how the vTEC and sTEC are related.

$$vTEC = \frac{sTEC - [b_R + b_S]}{S(\theta_I)} \quad (3)$$

where b_R and b_S are receiver and satellite biases, respectively. θ_I is the elevation angle in degrees, $S(\theta_I)$ is the obliquity factor with zenith angle ψ at the Ionospheric Pierce Point (IPP):

$$S(\theta_I) = \frac{1}{\cos \psi} = \left\{ 1 - \frac{R_E \cos \theta_I}{R_E + h} \right\}^{-1/2} \quad (4)$$

Where R_E is the Earth radius in km and $h = 350$ km is the ionospheric shell above the earth's surface.

Using a software developed by Gopi K. Seemala, publicly available at <https://seemala.blogspot.com/>, we computed the slant TEC (sTEC) and vertical TEC (vTEC) for a several number of GPS satellites, each one identified with a PseudoRandom Noise code (PRN). An example of such TEC calculations is shown in figure 3.1. The behavior of the TEC curve is due to many factors, including the earth's rotation, solar activity, etc. TID's and wave-like features are not as prominent and

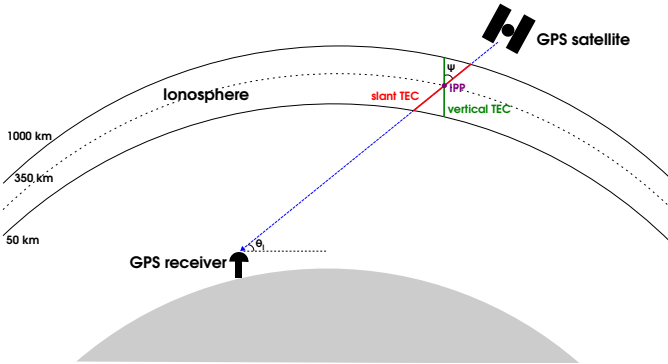


Fig. 2. Schematic figure of TEC calculations in the ionosphere. The GPS satellite is located at an elevation of θ_I from the position of the receiver. The Ionospheric Pierce Point (IPP) is located at a height of $h = 350$ km above the Earth's surface. ψ is the zenith angle. sTEC is measured along the satellite-receiver path and vTEC is measured in the radial direction sharing the same IPP as the satellite-receiver path.

are difficult to see. Since our sample is quite large, detrending process must be automatized in some degree, and it is critical to do this process adequately to have a correct interpretation of data (Maletckii et al., 2020).

3.1. Detrending process

For detrending our data we used a method developed for detecting plasma bubbles in the equatorial region (Pradipta et al., 2015), but proved to be effective for detecting Acoustic Gravity Waves (AGWs) and Traveling Ionospheric Disturbances (TIDs). With this method we are able to infer the trend from our TEC data using a Savitsky-Golay filter. However, the results of this filtering are sensitive to the parameters we use for such filtering, thus altering significantly the quality of the detrended signal. The TEC time series are assumed to be an additive combination of a signal and a trend (Maletckii et al., 2020). Thus we tested the method of Pradipta et al. (2015) over the sum of a known signal and a known trend and find the parameters of the Savitsky-Golay filter that recover in the best way the original signal. We used a test signal with the purpose to find out the most appropriate parameters for the filter and we show its functional form in appendix Appendix B.

On the other side, not necessarily all satellites could have detected ionospheric perturbations produced by TIDs, most of them should have detected other non related phenomena. To check which satellites have the best probabilities of detecting TIDs we compared in an azimuth-elevation map the satellites trajectory against the bolide trajectory. To do so we converted the bolide coordinates. The procedure is shown in Appendix C.

From Chelyabinsk event (Yang et al., 2014) we learned that high frequency TIDs (1.0 - 2.5 mHz) may travel at speed of $\sim 362 \pm 23$ m s $^{-1}$. Using this upper bound (since this event being less energetic, we can expect that similar TIDs in this case would travel at lower speed), we estimated the sphere where the TIDs should have propagated after a certain time interval. These propagation circles are shown in our azimuth-elevation maps.

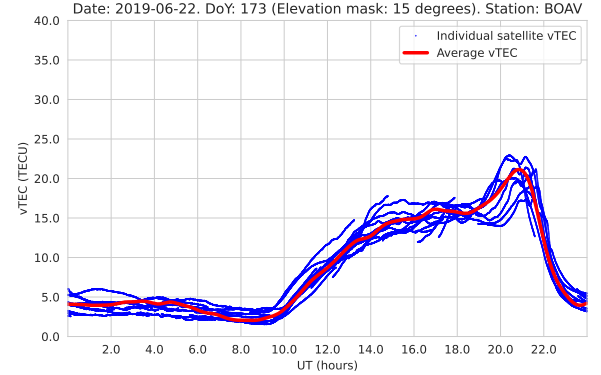


Fig. 3. Example of vTEC curves obtained for GPS data from BOAV station.

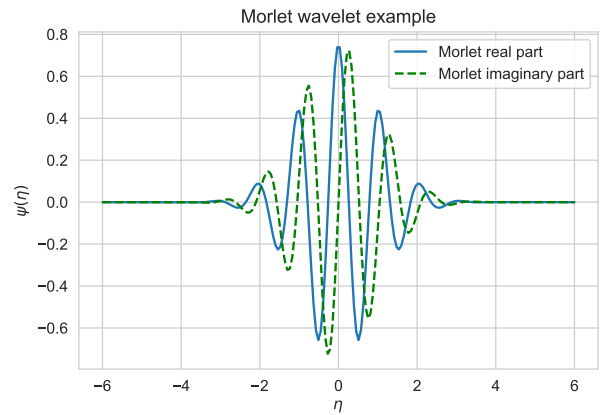


Fig. 4. Example of Morlet wavelet. Since this is a complex function, we show in blue continuous curve the real part and in green dashed curve the imaginary part. The Morlet wavelet consist in a sinusoid function with a determined frequency and damped to the left and right by a gaussian.

From these figures that are representative of the trajectories observed for all stations we can see that the bolide is observed at an elevation of about 80 degrees and that the satellite that consistently was closest to the bolide trajectory is PRN 13, but after a few hours, PRN 2, PRN 17 and PRN 19 could intercept TIDs as they propagate from the bolide.

3.2. Morlet Wavelet

From our time series, we must distinguish some features that should appear if any TIDs has been detected. The TIDs are wave-like features constrained in a limited amount of time. A function that fits this description is the Morlet wavelet, which is given by (Torrence & Compo, 1998):

$$\Psi_0(\eta) = \pi^{-1/4} \exp(i\omega_0\eta) \exp(-\eta^2/2) \quad (5)$$

Where ω_0 is a non-dimensional frequency, usually set to be 6 to satisfy the admissibility condition (Farge, 1992) and η is a non-dimensional "time parameter". The real and imaginary part of the Morlet wavelet is shown in figure 4.

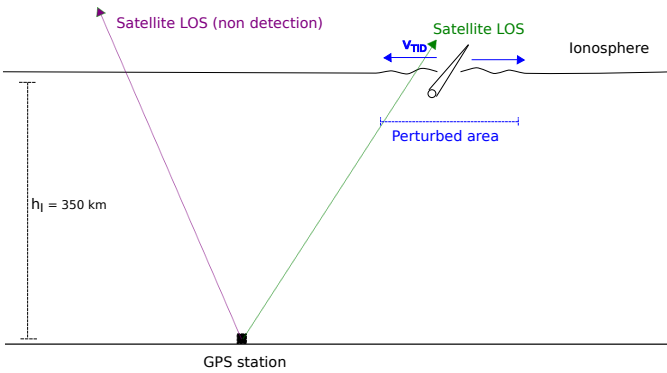


Fig. 5. TIDs generation sketch. When the bolide passes through the atmosphere perturbs the gas in its way. The resulting TIDs can be detected before the bolide fragmentation.

Table 2. Caribbean meteor possible physical properties obtained with algorithm , assuming a density of 3000 kg m^{-3}

| | |
|-------------------|--------------------------|
| Initial Velocity | 19.9 km s^{-1} |
| Initial mass | 340 kg |
| Entry angle (deg) | 64 |

3.3. TIDs velocity estimation

In figure 5 we sketch the scenario where TIDs may be generated. This model explains that when the bolide enters the atmosphere perturbs the gas in its path. The bolide passes through the ionosphere before fragmentation then the TIDs generated should have been detected before fragmentation, too. The delay time in this case depends now in the bolide velocity as it penetrates the atmosphere.

4. Meteor physical parameters

Using the estimation of the meteor energy and velocity from table 1, the trajectory angle estimated in appendix Appendix A from the velocity components of 64.4° and assuming the meteor has a density of 3000 kg m^{-3} , consistent with the composition of *condrites* (we must assure or edit this last statement), we estimated the initial velocity, initial mass and entry angle using (add citation and more text and once got the references) ...

5. Ionospheric background and sTEC time series

Ionospheric perturbations also can take place due to space weather and geomagnetic storms. So, in order to discard such events we investigated the space weather in the day each event occurred. We investigated the solar wind conditions in the event day and the previous 7 days, the x-ray flux and the Dst index at the event date.

5.1. Dst Index

We obtained measurements of Dst Index from WDC for Geomagnetism, Kyoto DST index service (<https://wdc.kugi.kyoto-u.ac.jp/dstdir/>), and is shown in figure 6. We see

that Dst index remains practically constant around zero, which confirms that there were not geomagnetic storms that could prevent us from detecting TIDs in our GPS data.

5.2. Solar wind

Another source of “space weather noise” that we should discard is unusual solar wind behavior or even coronal mass ejections. We collected data from the Deep Space Climate Observatory (DSCOVR) of solar wind speed, temperature, density, dynamic pressure and solar magnetic field, in order to monitor the solar wind behavior in the day of the event and the previous 6 or 7 days.

We were concerned of shock waves produced by rapid wind reaching slow wind, which also may produce TIDs and thus contaminating our GPS data, and may not be distinguishable from TIDs produced by the meteor passage. To check the presence of such shock waves, we estimate the relative velocity of solar wind of one day respect the previous one. The results are shown in figure 7, where we see that this velocity is almost constant and gives no chance for a fast stream reaching a slow one producing a shock wave.

5.3. X-rays flux

X rays are a clear source of ionization, they are generated mainly in the corona due to magnetospheric activity. A sudden increase of the flux or sudden variations may be a source of GW or giving appearance of GW. We investigated the X ray flux from the Sun at the event date and the previous week and collected data from the NOAA Space Prediction Center. X-rays flux remained constant in the time range we collected data.

5.4. dTEC and W index

Finally we wanted to check the effects of solar cycle variations. The critical frequencies of reflection f_c is proportional to the number of sunspots in the Sun, thus affecting our TEC measurements. Seasonal variations may be important too, since solar flux varies as the Earth revolves around the Sun. To measure these effects, we computed dTEC, defined as:

$$dTEC = \log_{10} \frac{TEC}{medTEC} \quad (6)$$

Where TEC is the average TEC measurements of a certain day, while $medTEC$ is the median TEC of the 27 previous days, corresponding to the solar rotation period. dTEC was computed for the event day with each station. The W index reveals TEC behavior and the ionospheric perturbation level. In table 3 we show the W index levels, the corresponding dTEC and how perturbed is the ionosphere.

We estimated the dTEC and the corresponding W index for all the GPS stations from we collected data. An example is shown in figure 8. In this figure we see how dTEC changes in time on the meteor date. The moment the meteor fragmented is shown with a black dashed line. The W index values are shown as the colored background.

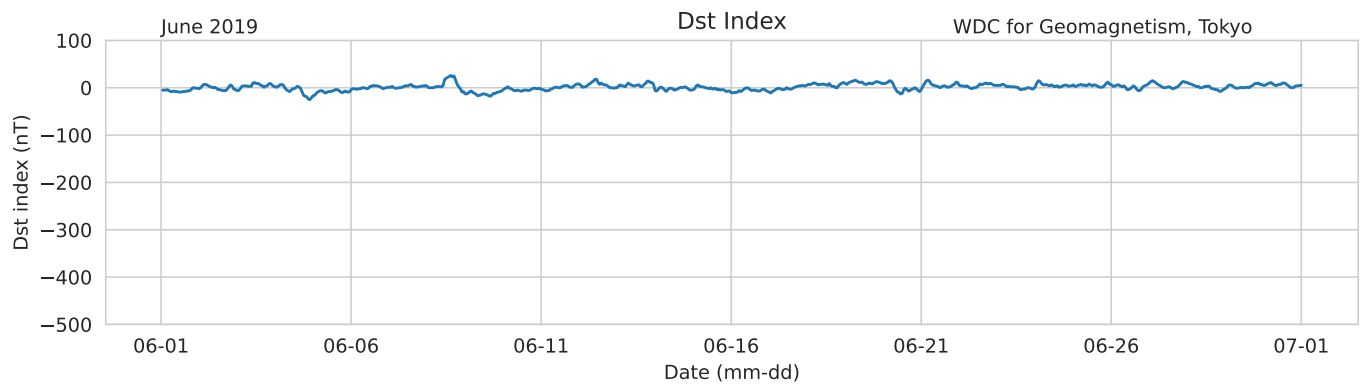


Fig. 6. Dst index for 2019 June 22th. Data obtained from WDC for Geomagnetism, Kyoto DST index service.

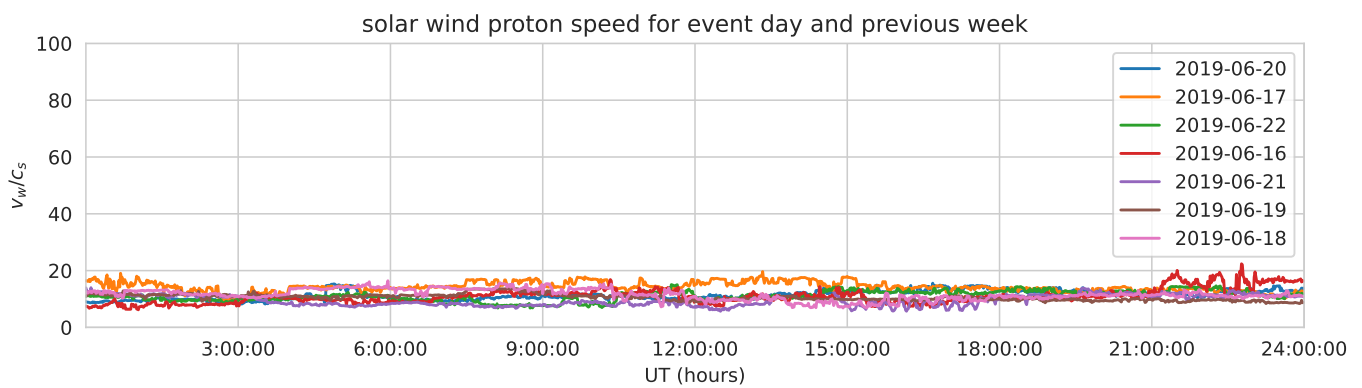


Fig. 7. Relative speed of solar wind at the event day and previous week respect the previous day, normalized with speed of sound. Each curve represents one day data.

Table 3. W index values with their corresponding dTEC values and a brief description of the ionospheric state when that index is obtained.

| dTEC | W index | Ionospheric state |
|--------------------------|---------|-----------------------|
| $dTEC = 0$ | 0 | Reference quiet state |
| $0 < dTEC < 0.046$ | ± 1 | Quiet state |
| $0.046 < dTEC < 0.155$ | ± 2 | Weak perturbation |
| $0.155 < dTEC < 0.301$ | ± 3 | Moderated storm |
| $ dTEC > 0.301$ | ± 4 | Intense storm |

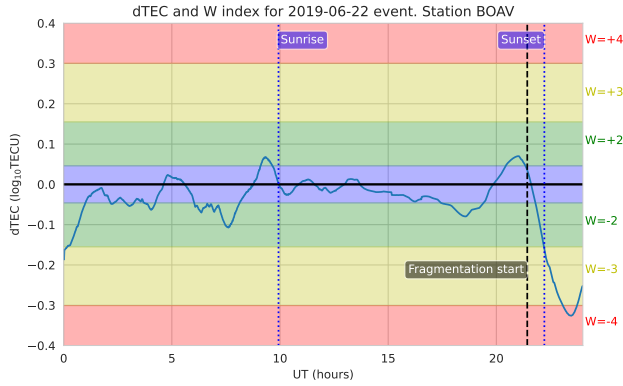


Fig. 8. dTEC and W index for station BOAV. dTEC is shown as the continuous blue curve. The corresponding W index ranges are shown as the colored backgrounds, from quiet state in blue to strong storm ($|W| = 4$) in red. The meteor fragmentation time is shown in vertical dashed line, and as additional information the local sunrise and sunset in dashed blue lines.

In this example and most of the stations we noted that the W index stands in negative values from -2 to -3 and normalizes to 1 after the 10 hrs. To understand the origin of this behavior we also included the local sunrise and sunset, and we found out that W index is quite negative at night, and normalizes after sunrise (local night occurs from 21-23 hrs of previous day to ~ 10 hrs, check table D.4 for accurate information). Also found out that meteor fragmentation occurred a few hours before sunset, depending on the station. The high fluctuations in the dTEC may be attributable to the fact that at nighttime the logarithm is more susceptible to small variations since TEC is closer to zero. Fluctuations normalize after sunrise.

5.5. Solar terminator

If a meteoroid passage and explosion occurs at sunrise or sunset, the passage of the solar terminator should be taken into account since it is one of the GW sources and cause some disturbances in the ionosphere (Somsikov, 2011). In figure 9 we see that meteor fragmentation occurred outside the solar terminator, but some GPS stations (KOUG and KOUR) are located very close to (sunset comes about 20 minutes after the fragmentation). In order to distinguish between the effects of the meteor and the solar terminator we detrended GPS data for the mentioned stations at dates prior of the meteor fall, those dates are close enough to guarantee that the sunset occurs almost at the same time. With this we can isolate the effects of the solar terminator and analyze its effects to check how they affect

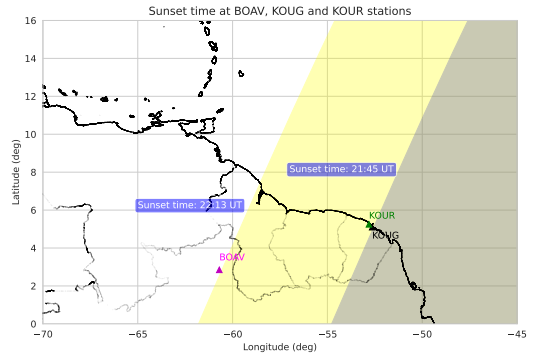


Fig. 9. Solar terminator position for the most southern stations: BOAV (yellow shadow), KOUG and KOUR (gray shadow). The corresponding sunset times are labeled in the corresponding terminator line, and the sunset time difference between KOUG and KOUR stations is just 2 minutes. Sunset time in stations KOUR and KOUG occurred 20 minutes later than meteor fragmentation.

into our time series. Some results are shown in figure 10 for station KOUG, PRNs 2 and 12. In these cases we see that the solar terminator does perturb the ionosphere, and its effects can bypass the detrending process, since they consist in wave-like variations of TEC. But these perturbations most of the time are weaker and distinguishable from the perturbations produced by the meteor passage, so we can safely assume that they don't affect in our detections. Even more, comparing time series from previous days we can help us to discriminate between time series with detected TID from others where only noise is recorded since some patterns in the time series can be detected. Time series too similar with the previous days can be classified as non detections.

5.6. sTEC time series

We detrended the RINEX data we obtained for all stations and analyzed separately each satellite-receiver time series in order to find by visual inspection wave-like features. We must be careful when making conclusions about the presence of TIDs produced by the bolide in the cases when the sunset and the fragmentation occurred in a short period of time. We separated those time series where we detected the presence of such features (see §3.2), from all the others, which could be too noisy, too few data, etc. A significant sample of about 10% of all the time series we have are shown in figures 11-13.

In order to check which stations actually observed the TIDs generated by the bolide fragmentation, we proceeded to learn which stations were located near the bolide trajectory at the event time or the next few hours. Stations located far of the bolide trajectory are more likely to have detected other phenomena not related with the bolide passage. Since we are using sTEC measurements, we want to have a picture of the line of sight we are considering in our sTEC measurements. To do such task we will compare the bolide trajectory with all of the satellites in local coordinates (azimuth and elevation) to see if at least one was close enough to the bolide trajectory and its elevation. Such diagrams are shown in figures for the same stations

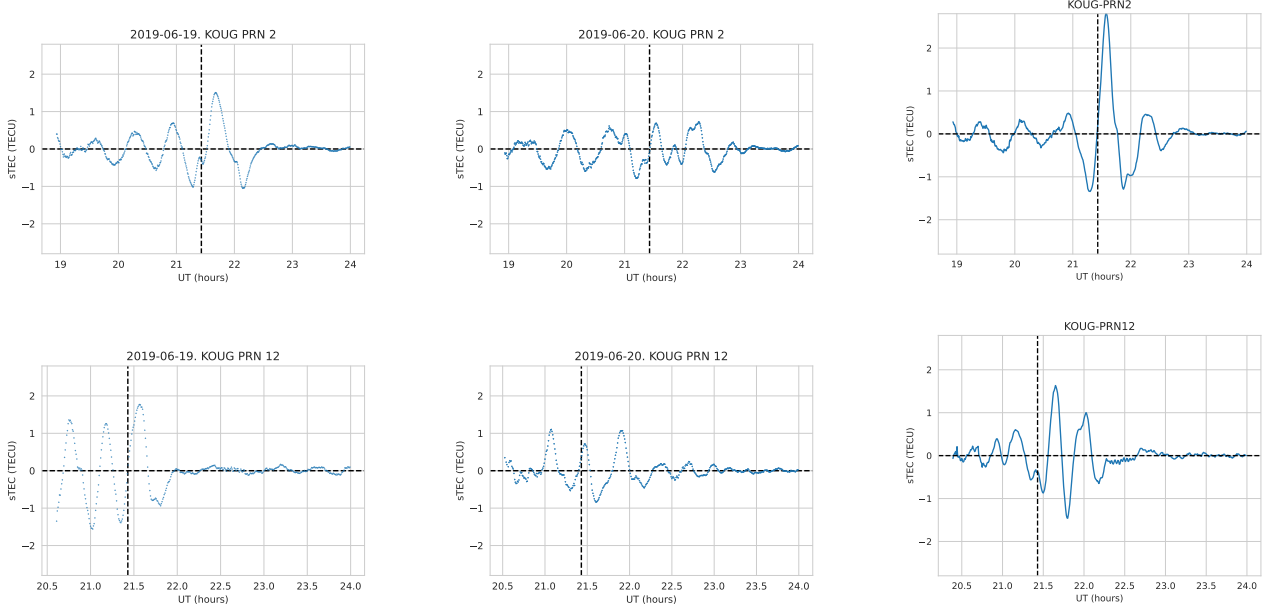


Fig. 10. Detrended sTEC time series for station KOUNG for the days 2019-06-19, 2019-06-20 and 2019-06-22 (three days before meteor fall, two days and the meteor fall date, from left to right). The satellite receiver LOS with PRN 2 is in top, and the LOS with PRN 12 is in bottom.

of figures 11 - 13. Ideally if the satellite trajectory intersects the meteor trajectory in our TEC series we see the TEC variations in the line of sight where the meteor passed. But it is also possible that a slightly distant satellite detected some TIDs that propagated away from the source.

6. Discussion and conclusions

We collected data for a sample of GPS station from UNAVCO network around the Caribbean bolide was detected in the same day and next day. We used data from the GLM, where the total energy was estimated from light curves, and USG sensors, where energy data is available to spot the bolide position and estimate the trajectory at the fragmentation instant. For GPS data, we adapted the method from Pradipita et al. (2015) for detrending all the resultant TEC curves to remove the effects of Earth rotation and solar activity and make the wave-like features more evident. In order to discriminate which stations made a detection from the ones who didn't, we compared the detrended time series with a Morlet wavelet. We discarded other sources of GWs such like slow solar wind reached by fast wind, fluctuations in solar X-rays, coronal mass ejections and solar terminator effects. We found TIDs features in sTEC series from stations CN04, CN40, GRE1, TTSF, TTUW, BOAV, KOUNG and KOUR stations with at least one satellite.

7. Acknowledgments

The author Tarango-Yong thanks to DGAPA-UNAM by the posdoctoral fellowship, as well as the Laboratorio de Ciencias Geoespaciales (LACIGE) from the Escuela Nacional de Estudios Superiores – Morelia for the facilities provided to

carry out the calculations of this paper. In addition, Gutiérrez-Zalapa wishes to thanks the Consejo Nacional de Ciencias y Tecnología (CONACyT) for the support in carrying out this research, he also wishes to thanks the Posgrado en Ciencias de la Tierra from the Universidad Nacional Autónoma de México. Finally, M. Rodríguez-Martínez also is grateful for the DGAPA PAPIIT/PAPIME projects (IN118119/PE103419) to the computing support.

Appendix A. Bolide velocity components

The USG database from JPL is a great source of information about the brightest bolides that have entered the atmosphere since 1988. However, the velocity components (v_x, v_y, v_z) are displayed in a geocentric Earth-fixed reference frame explained as follows:

v_x lies in the Earth's equatorial plane, parallel to the equator and points towards the prime meridian, v_z is parallel to the earth's rotational axis and points towards the north celestial pole and v_y completes the right-handed reference system. Figure shows graphically these velocity components.

In the other hand, it might be useful and more intuitive to describe the velocity components in terms of the local reference system composed by (v_{lon}, v_{lat}, v_h), where v_{lon} is the velocity component parallel to the equatorial plane, positive towards east, v_{lat} is parallel to the polar plane, positive to north, and v_h is the radial component pointing towards the center of Earth. Figure A.16 sketches both reference systems simultaneously.

The transformation between both reference systems in the north-west hemisphere is given as follows:

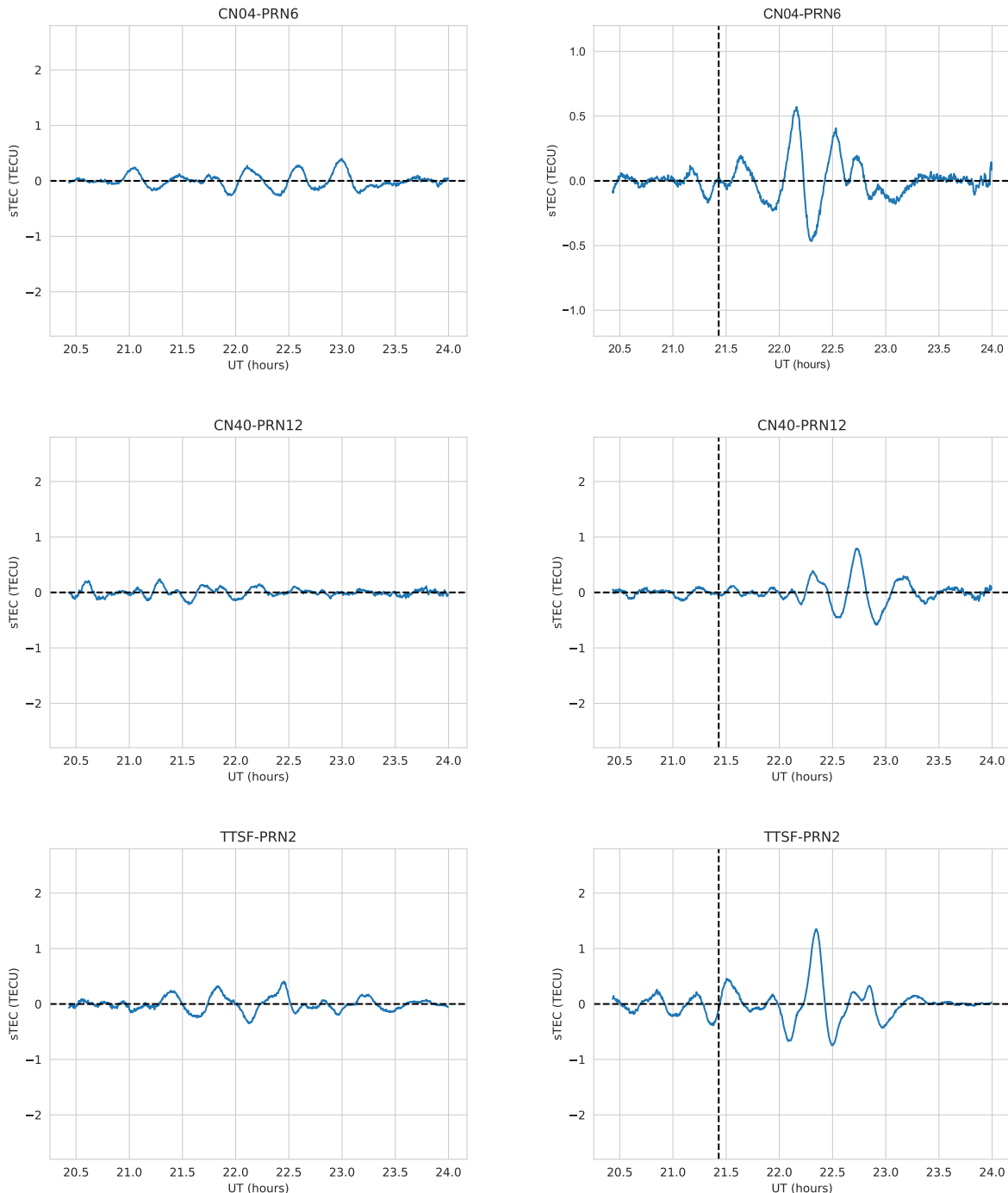


Fig. 11. sTEC time series for stations where TIDs are likely to be detected. In the left panels we show the time series for the previous day of meteor fall, and in the right panels the time series for the meteor fall date.

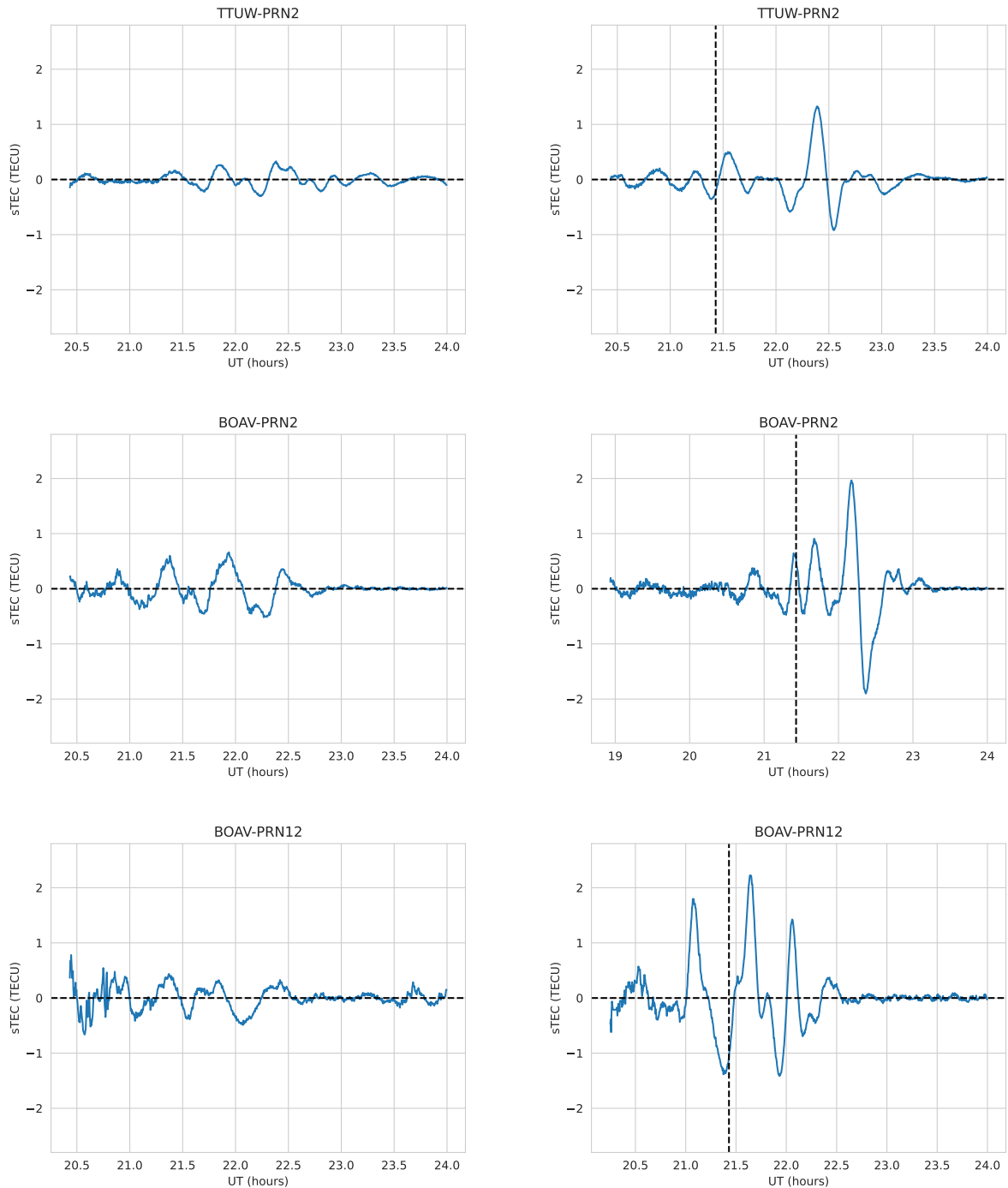


Fig. 12. Continuation of figure 11

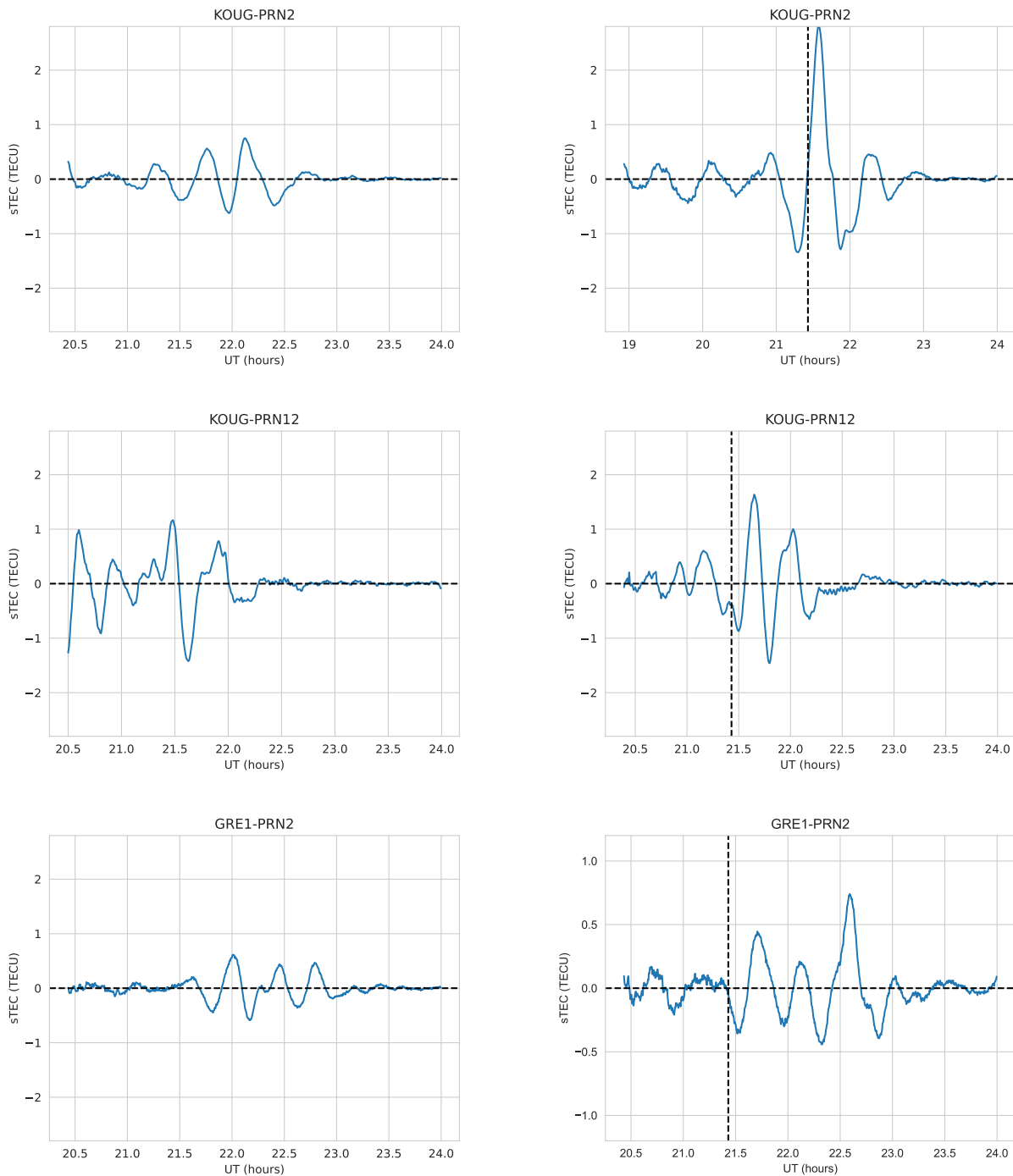


Fig. 13. Continuation of figures 11 and 12.

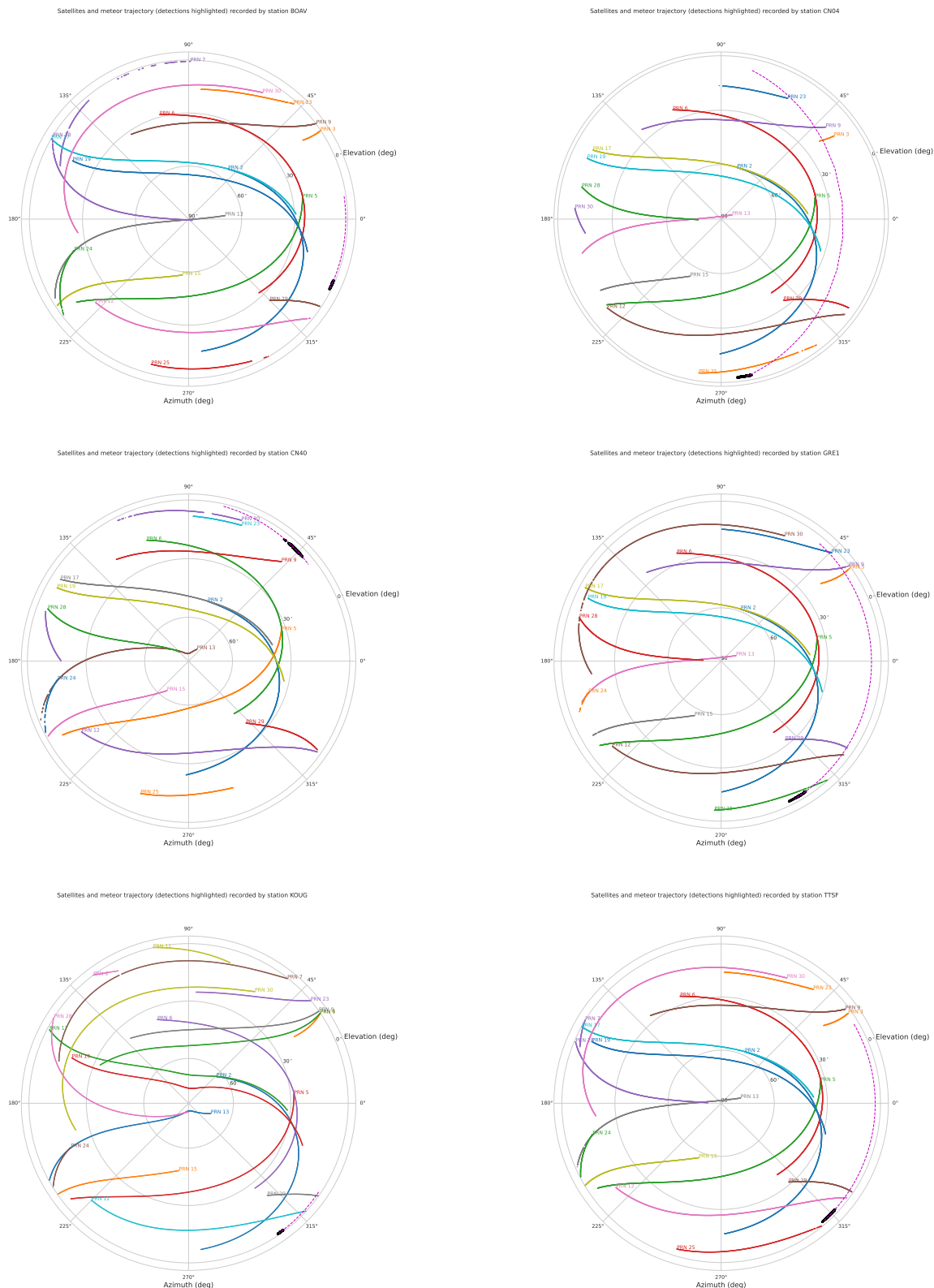


Fig. 14. Azimuth-Elevation maps for GPS stations which presumably detected TIDs. In colored curves we show the satellites trajectories with their respective label. The black dots are the meteor trajectory using the GLM data and the magenta dashed curve represent the meteor trajectory using the velocity parameters from table 1.

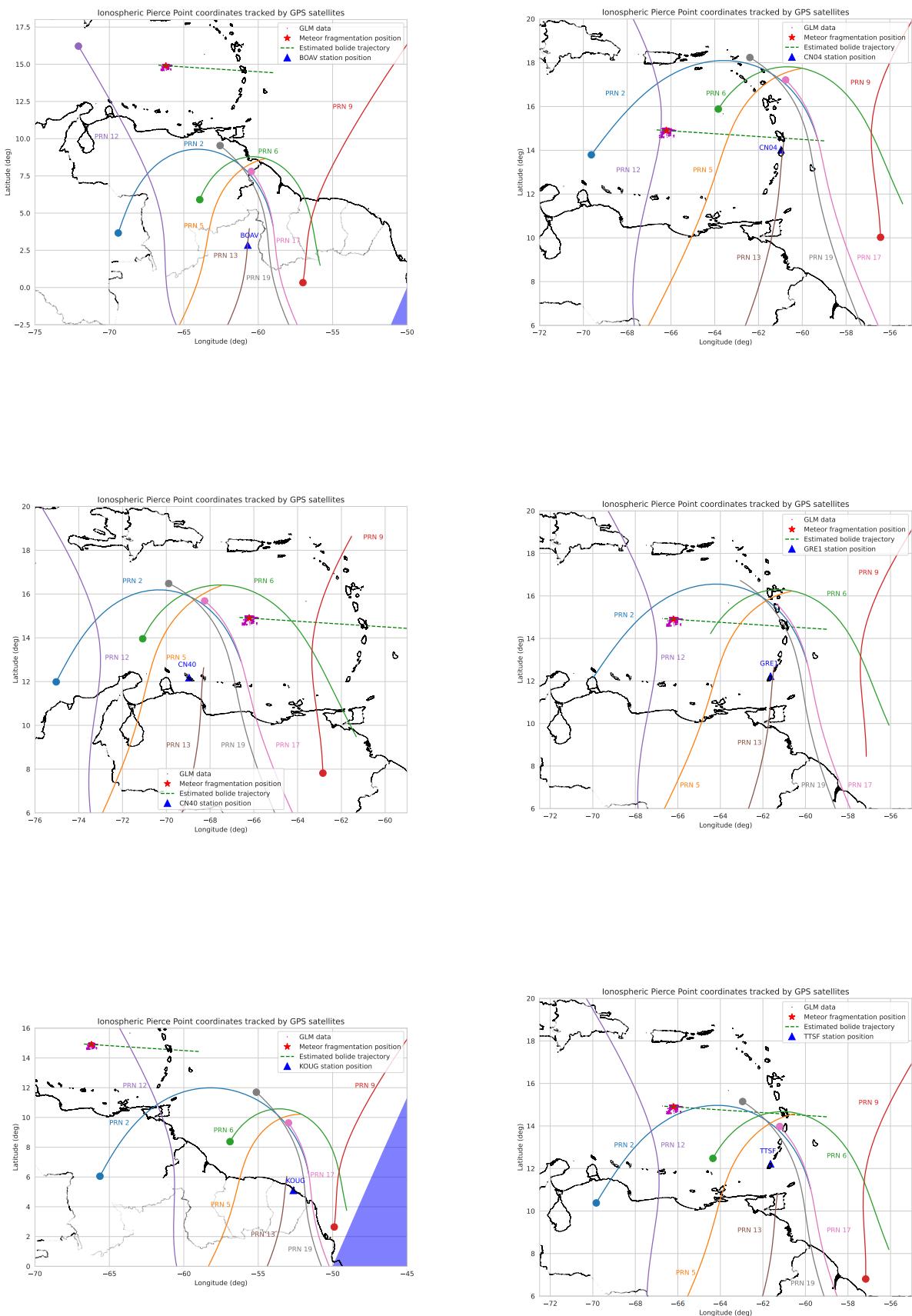


Fig. 15. Position of IPP in the satellite receiver LoS for the same GPS stations as figure 5.6. The GLM data are shown in magenta dots, the fragmentation position

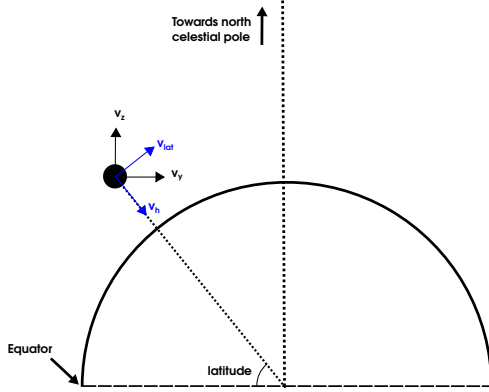


Fig. A.16. Velocity components of bolide. The geocentric Earth fixed reference system is sketched in black and the local spherical reference system in blue. The components parallel to the equatorial plane are not shown since are perpendicular to the plane of the page.

$$v_{lon} = v_x \quad (\text{A.1})$$

$$v_{lat} = v_z \cos L - v_y \sin L \quad (\text{A.2})$$

$$v_h = v_y \cos L + v_z \sin L \quad (\text{A.3})$$

Where L is the bolide latitude. With this information, we can estimate the velocity tangential to the Earth's surface as $v_{tan} = ((v_{lon})^2 + (v_{lat})^2)^{1/2}$ and finally the trajectory angle respect to the normal as $\tan \theta = \frac{v_{tan}}{v_h}$. Using equations (A.1) to (A.3) we obtain the following:

$$v_{tan} = ((v_x)^2 + (v_z \cos L - v_y \sin L)^2)^{1/2} \quad (\text{A.4})$$

$$\tan \theta = \frac{((v_x)^2 + (v_z \cos L - v_y \sin L)^2)^{1/2}}{v_y \cos L + v_z \sin L} \quad (\text{A.5})$$

Substituting the corresponding data from table 1 into equation (A.5) we find that that the trajectory angle of the meteor respect to the normal is $\theta \approx 64.4^\circ$

Appendix B. Detrending test signal

Figure B.17 shows the form of this test time series, described mathematically as follows (Maletckii et al., 2020):

$$I_R(t) = A \cdot \exp \left[-0.5 \left(\frac{t - t_m}{d_t} \right)^2 \right] \cdot \sum_n^i \sin(\omega_i t) \quad (\text{B.1})$$

$$\text{Trend}(t) = B \cdot |t - t_0|^3 \quad (\text{B.2})$$

Where equation (B.1) is the signal we want to detrend and equation (B.2) is the trend we want to remove. A is the amplitude of the signal, set as 0.2 TECU, t_m is a parameter which determines the position of the envelope maximum, set as 250 min, which is the half of the array length, d_t is the half width of the envelope, set as 50 min and ω_i are the frequencies of three harmonics with periods of 20 min, 40 min and

60 min. In the other hand, B is the amplitude of the trend, set as 3.84×10^{-6} TECU min⁻¹ and $t_0 = 250$ min determines position of the minimum of the trend.

For the detrending we used a Savitsky-Golay filter of order 3, this is lowest order filter which at the same time avoids too much oscillations and allows to the fit (and its derivative) to be smooth. The other remaining parameter is the window size, i.e. the number of convolution coefficients necessary for the regression, which must be an odd integer, greater than the order of the polynomial order and lower than the array size. Then, we estimated the detrended signal using all possible values for the window size and estimated the residuals as follows:

$$\text{residuals} = \sum_i^N (d_i - s_i)^2 \quad (\text{B.3})$$

Where N is the array size, d_i is the value of the detrended signal at the time t_i and s_i is the reference signal at the same time. In figure we show the behavior of residuals as a function of the window size relative to the array size. We noted that the residuals behavior is almost insensitive to the window size when its size is lower than than 60% of the array size, when the errors start to grow exponentially, but going to more detail, we found that using a window size of about 1/4 of the array length, such errors are minimal. The detrended test curve is shown in figure Appendix B, compared with the original signal, as well as the subtraction of both curves. In an ideal situation it should be zero for all times, but even in this case the amplitude of the envelope is about the tenth part of the amplitude of the envelope of the signal.

Appendix C. Coordinates transformation

In order to change coordinates form geocentric to local coordinates for the bolide position, we may assume the flat earth approximation since the GPS stations we used in our work are located near the place the bolide was detected, and the apparent curvature of Earth at the bolide height is almost zero. With this in mind, in figure C.19 we show the flat Earth approximation in order to transform the geocentric coordinates of the bolide (latitude and longitude) to their corresponding local coordinates azimuth and elevation. With the aid of this image, we derive the following equations:

$$\tan Az = \frac{\Delta\lambda}{\Delta L} \quad (\text{C.1})$$

$$\tan Ele = \frac{h}{r} \quad (\text{C.2})$$

Where $r = R_E (\Delta L)^2 + (\delta\lambda)^2)^{1/2}$ and $(\delta L, \delta\lambda)$ are the separation in latitude and longitude of the bolide from the GPS station, respectively. Azimuth is measured from the north counterclockwise and elevation is measured from the Earth's horizon to zenith, in such way azimuth goes from 0° to 360° and elevation from 0° to 90°.

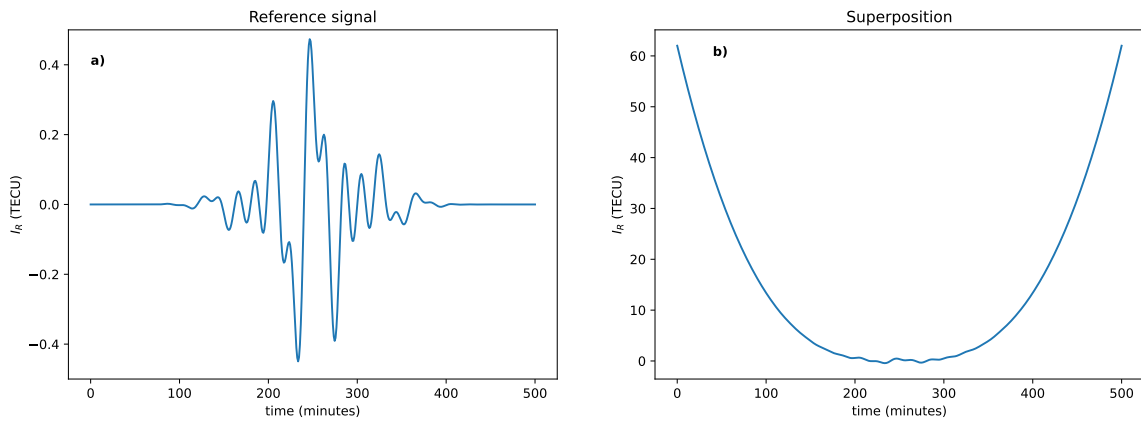


Fig. B.17. Initial setup for testing detrending method. a) Reference signal given by equation (B.1). b) Superposition between a) and the trend given by (B.2)

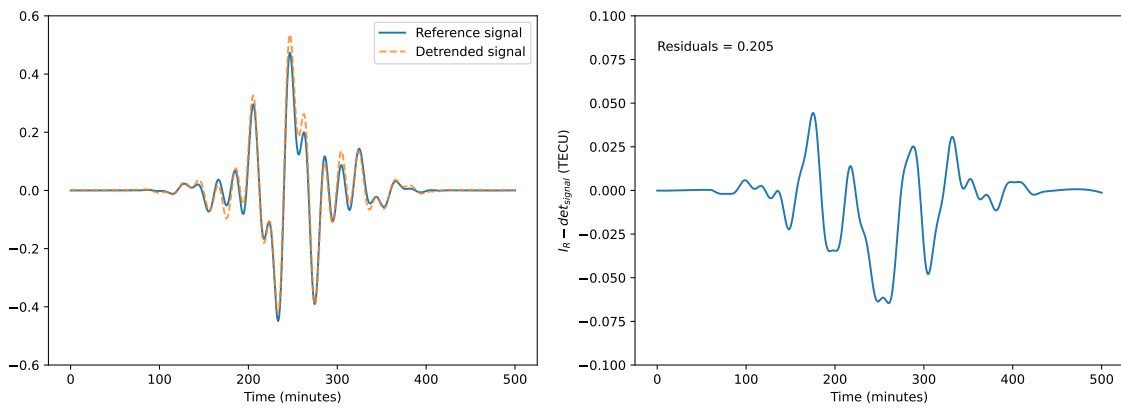


Fig. B.18. Left: Original test signal (blue continuous curve) compared with the result of detrending the superposition of the test signal with the test trend (figure B.17b), which is the orange dashed curve. Right: Subtraction of both curves of left side. The amplitude of the envelope of this residuals qualitatively is about tenth percent of the amplitude of the original signal.

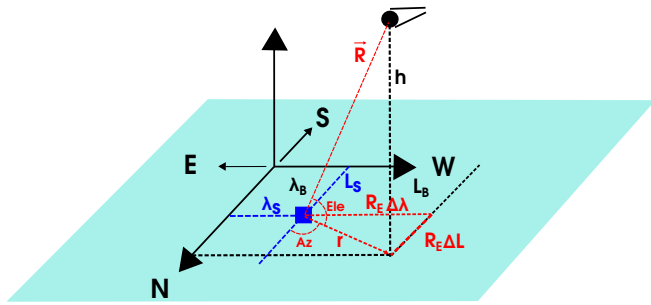


Fig. C.19. Sketch of flat Earth approximation for transforming the fireball position from geocentric coordinates to local coordinates. From this picture we can derive equations (4) to (6) to estimate the local azimuth and elevation of the bolide at the GPS station position. \vec{R} is the vector pointing to the bolide position with origin in the GPS station. r is the projection of \vec{R} in the Earth's plane. L_s and L_B are the latitudes of the station and the bolide, respectively, while λ_s and λ_B their longitudes, h is the bolide height and R_E the radius of Earth.

Appendix D. UNAVCO Acknowledgements and stations list

In table we will enlist the stations from we collected data for our work. This material is based on services provided by the GAGE Facility, operated by UNAVCO, Inc., with support from the National Science Foundation and the National Aeronautics and Space Administration under NSF Cooperative Agreement EAR-1724794, we are deeply grateful with all the people that was involved and whose work we are citing here.

Table D.4. List of GPS stations used for this work.

| Station name | Latitude (deg) | Longitude (deg) | Citation |
|--------------|----------------|-----------------|---|
| AIRS | 16.74 | -62.21 | https://doi.org/10.7283/T53B5XGJ |
| BARA | 18.21 | -71.09 | None available |
| BOAV | 2.85 | -60.70 | None available |
| CN00 | 17.67 | -61.79 | https://doi.org/10.7283/T5FN14GQ |
| CN04 | 14.02 | -60.97 | https://doi.org/10.7283/T5BP0124 |
| CN05 | 18.56 | -68.35 | https://doi.org/10.7283/T5VQ30ZH |
| CN19 | 12.61 | -70.04 | https://doi.org/10.7283/T5HD7S2B |
| CN27 | 19.67 | -69.93 | https://doi.org/10.7283/T5JD4V2P |
| CN40 | 12.18 | -68.96 | https://doi.org/10.7283/T5BV7DWT |
| CRLR | 18.41 | -68.93 | https://doi.org/10.7283/T5FN14JM |
| CRSE | 18.76 | -69.04 | None available |
| GERD | 16.80 | -62.19 | https://doi.org/10.7283/T5TT4PBT |
| GRE1 | 12.22 | -61.64 | https://doi.org/10.7283/T5BC3WZ5 |
| JME2 | 18.23 | -72.54 | https://doi.org/10.7283/T5KW5D38 |
| KOUG | 5.10 | -52.64 | None available |
| KOUR | 5.25 | -52.81 | None available |
| LVEG | 19.22 | -70.53 | https://doi.org/10.7283/T5CZ35GC |
| NWBL | 16.82 | -62.20 | https://doi.org/10.7283/T5ZK5F13 |
| OLVN | 16.75 | -62.23 | https://doi.org/10.7283/T5Q23XMD |
| RCHY | 16.70 | -62.15 | https://doi.org/10.7283/T5707ZSJ |
| RDAZ | 18.45 | -70.72 | None available |
| RDF2 | 19.45 | -70.68 | None available |
| RDHI | 18.60 | -68.72 | None available |
| RDLT | 19.31 | -69.55 | https://doi.org/10.7283/T5J101GT |
| RDMA | 19.54 | -71.08 | https://doi.org/10.7283/T50863NM |
| RDMC | 19.85 | -71.64 | None available |
| RDMS | 18.98 | -69.04 | https://doi.org/10.7283/T5DV1HPQ |
| RDNE | 18.50 | -71.42 | None available |
| RDON | 16.93 | -62.35 | https://doi.org/10.7283/T5W37TFB |
| RDSD | 18.46 | -69.91 | https://doi.org/10.7283/T5CZ3594 |
| RDSF | 19.29 | -70.25 | None available |
| RDSJ | 18.82 | -71.23 | https://doi.org/10.7283/T59W0CTW |
| SPED | 18.46 | -69.31 | https://doi.org/10.7283/T5HQ3X75 |
| SROD | 19.48 | -71.34 | https://doi.org/10.7283/T5862DSD |
| TGDR | 18.21 | -71.10 | https://doi.org/10.7283/T5222S3R |
| TRNT | 16.76 | -62.16 | https://doi.org/10.7283/T5K935W2 |
| TTSF | 10.28 | -61.47 | https://doi.org/10.7283/T5JQ0ZCJ |
| TTUW | 10.64 | -61.40 | https://doi.org/10.7283/T5TQ5ZTR |

References

- Dudorov, A. E., & Eretnova, O. V. (2020). The Rate of Falls of Meteors and Bolides. *Solar System Research*, 54(3), 223–235. doi:10.1134/S003809462003003X.
- Emery, W., & Camps, A. (2017). Chapter 6 - remote sensing using global navigation satellite system signals of opportunity. In W. Emery, & A. Camps (Eds.), *Introduction to Satellite Remote Sensing* (p. 455–564). Elsevier. doi:10.1016/B978-0-12-809254-5.00006-3.
- Farge, M. (1992). Wavelet transforms and their applications to turbulence. *Annual Review of Fluid Mechanics*, 24(1), 395–458. doi:10.1146/annurev.fl.24.010192.002143.
- Goodman, S. J., Blakeslee, R. J., Koshak, W. J., Mach, D., Bailey, J., Buechler, D., Carey, L., Schultz, C., Bateman, M., McCaul, E., & Stano, G. (2013). The goes-r geostationary lightning mapper (glm). *Atmospheric Research*, 125-126, 34–49. doi:<https://doi.org/10.1016/j.atmosres.2013.01.006>.
- Jenniskens, P., Albers, J., Tillier, C. E., Edgington, S. F., Longenbaugh, R. S., Goodman, S. J., Rudlosky, S. D., Hildebrand, A. R., Hanton, L., Ciceri, F., Nowell, R., Lyytinen, E., Hladiuk, D., Free, D., Moskovitz, N., Bright, L., Johnston, C. O., & Stern, E. (2018). Detection of meteoroid impacts by the geostationary lightning mapper on the goes-16 satellite. *Meteoritics & Planetary Science*, 53(12), 2445–2469. doi:<https://doi.org/10.1111/maps.13137>.
- Kumar, D. S., Priyadarshi, S., Seemala, G., & Singh, A. (2012). Gps-tec variations during low solar activity period (2007-2009) at indian low latitude stations. *Astrophysics and Space Science*, 339, 165–178. doi:10.1007/s10509-011-0973-6.
- Maletckii, B., Yasyukevich, Y., & Vesnin, A. (2020). Wave signatures in total electron content variations: Filtering problems. *Remote Sensing*, 12(8). doi:10.3390/rs12081340.
- Pradipita, R., Valladares, C. E., & Doherty, P. H. (2015). An effective tec data detrending method for the study of equatorial plasma bubbles and traveling ionospheric disturbances. *Journal of Geophysical Research: Space Physics*, 120(12), 11,048–11,055. doi:<https://doi.org/10.1002/2015JA021723>.
- Somsikov, V. M. (2011). Solar terminator and dynamic phenomena in the atmosphere: A review. *Geomagnetism and Aeronomy*, 51(6), 707–719. doi:10.1134/S0016793211060168.
- Torrence, C., & Compo, G. P. (1998). A Practical Guide to Wavelet Analysis. *Bulletin of the American Meteorological Society*, 79(1), 61–78. doi:10.1175/1520-0477(1998)079<0061:APGTWA>2.0.CO;2.
- Wheeler, L. F., & Mathias, D. L. (2019). Probabilistic assessment of Tunguska-scale asteroid impacts. *Icarus*, 327, 83–96. doi:10.1016/j.icarus.2018.12.017.
- Yang, Y.-M., Garrison, J. L., & Lee, S.-C. (2011). Application of gnss networks to detect and analyze atmospheric-induced ionospheric disturbances coincident with earthquakes and tsunamis. In *2011 IEEE International Geoscience and Remote Sensing Symposium* (pp. 1131–1134). doi:10.1109/IGARSS.2011.6049396.
- Yang, Y.-M., Komjathy, A., Langley, R. B., Vergados, P., Butala, M. D., & Mannucci, A. J. (2014). The 2013 chelyabinsk meteor ionospheric impact studied using gps measurements. *Radio Science*, 49(5), 341–350. doi:<https://doi.org/10.1002/2013RS005344>.